

**Experimental, numerical and analytical investigations of masonry corners
Influence of the horizontal pseudo-static load orientation**

Colombo, Carla ; Savalle, Nathanaël ; Mehrotra, Anjali; Funari, Marco Francesco ; Lourenço, Paulo B.

DOI

[10.1016/j.conbuildmat.2022.127969](https://doi.org/10.1016/j.conbuildmat.2022.127969)

Publication date

2022

Document Version

Final published version

Published in

Construction and Building Materials

Citation (APA)

Colombo, C., Savalle, N., Mehrotra, A., Funari, M. F., & Lourenço, P. B. (2022). Experimental, numerical and analytical investigations of masonry corners: Influence of the horizontal pseudo-static load orientation. *Construction and Building Materials*, 344, Article 127969. <https://doi.org/10.1016/j.conbuildmat.2022.127969>

Important note

To cite this publication, please use the final published version (if applicable).
Please check the document version above.

Copyright

Other than for strictly personal use, it is not permitted to download, forward or distribute the text or part of it, without the consent of the author(s) and/or copyright holder(s), unless the work is under an open content license such as Creative Commons.

Takedown policy

Please contact us and provide details if you believe this document breaches copyrights.
We will remove access to the work immediately and investigate your claim.



Experimental, numerical and analytical investigations of masonry corners: Influence of the horizontal pseudo-static load orientation

Carla Colombo^a, Nathanaël Savalle^a, Anjali Mehrotra^{b,*}, Marco Francesco Funari^{a,c}, Paulo B. Lourenço^a

^a University of Minho, ISE, Guimarães, Portugal

^b TU Delft, Delft, the Netherlands

^c Department of Civil and Environmental Engineering, University of Surrey, Guildford GU2 7XH, UK

ARTICLE INFO

Keywords:

Limit analysis
Flexural mechanism
Rocking-sliding mechanism
Seismic assessment
Tilting tests
Dry-joint stiffness
Discrete element modelling

ABSTRACT

The present work aims to expand the knowledge of the behaviour of masonry corners, which are capital to obtain an integral seismic response in masonry buildings. In particular, the influence of the seismic load orientation (from $\pi/4$ to $\pi/2$) is investigated experimentally, numerically and analytically. Both units and interfaces have been subjected to a material characterisation process, following which pseudo-static 1:4 scaled experiments on a tilting table have been conducted on a symmetric dry-joint masonry corner. The experimental results have also been simulated using a discrete element model. Finally, a new analytical limit analysis model has been developed, which considers both experimental and numerical observations and accounts for rocking-sliding and flexural mechanisms. In general, a good agreement is found between the three approaches, both in terms of collapse mechanism and load multiplier.

1. Introduction

Simulation of the seismic behaviour of historical masonry structures is a challenging task. It depends on several factors, such as the mechanical properties of the constitutive materials (units and mortar), the geometrical configuration of the structure, the connections between load-bearing components, the stiffness of the horizontal diaphragms, etc. When an earthquake occurs, localised out-of-plane (OOP) failure mechanisms are prone to form in historical masonry structures, particularly in the absence of box-like or integral structural behaviour [1,2]. In this framework, following post-seismic damage surveys carried out after the Irpinia and Syracuse earthquakes in Italy, in [3], an abacus of local failure mechanisms was compiled that may be assessed through simple analytical formulations mainly based on the theorems of the limit analysis (LA).

Once a mechanism is selected, a set of equilibrated generalised forces and a set of compatible generalised virtual displacements are determined. Then, the work done by the generalised forces in equilibrium with the internal stresses for the given set of generalised virtual displacements is computed. The application of the static theorem leads to a

lower-bound or safe solution based on equilibrium equations, while the application of the kinematic theorem provides an upper-bound multiplier of the collapse load factor [4]. Thus, the solution that satisfies the hypotheses of the pre-mentioned theorems and equilibrium, compatibility and material conditions is the correct solution and provides the theoretical actual collapse load multiplier for the specific problem. In the last decade, following Heyman's pioneering work [4], to investigate the most reasonable collapse mechanisms, different algorithms were implemented into user-defined routines of analysis, adopting the lower or upper bound theorem of LA [5–8].

Among the damage mechanisms found in masonry structures, failure of masonry corners is commonly observed during earthquakes [9,10]. Certain geometrical features or structural details usually increase the probability of corner failure, among them: i) the lack of confinement of the building by adjacent structures, ii) the presence of openings, iii) the presence of chimneys, and iv) the lack of rigid horizontal diaphragms. However, limited investigations have been conducted concerning the seismic vulnerability of masonry corners. To that end, in [5], an analytical formula based on LA was proposed to determine masonry corners' associated horizontal load multiplier. A similar methodology

* Corresponding author.

E-mail addresses: carla.colombo95@gmail.com (C. Colombo), n.savalle@civil.uminho.pt (N. Savalle), A.A.Mehrotra@tudelft.nl (A. Mehrotra), m.funari@surrey.ac.uk (M.F. Funari), pbl@civil.uminho.pt (P.B. Lourenço).

<https://doi.org/10.1016/j.conbuildmat.2022.127969>

Received 15 February 2022; Received in revised form 16 May 2022; Accepted 24 May 2022

Available online 1 July 2022

0950-0618/© 2022 The Authors. Published by Elsevier Ltd. This is an open access article under the CC BY license (<http://creativecommons.org/licenses/by/4.0/>).

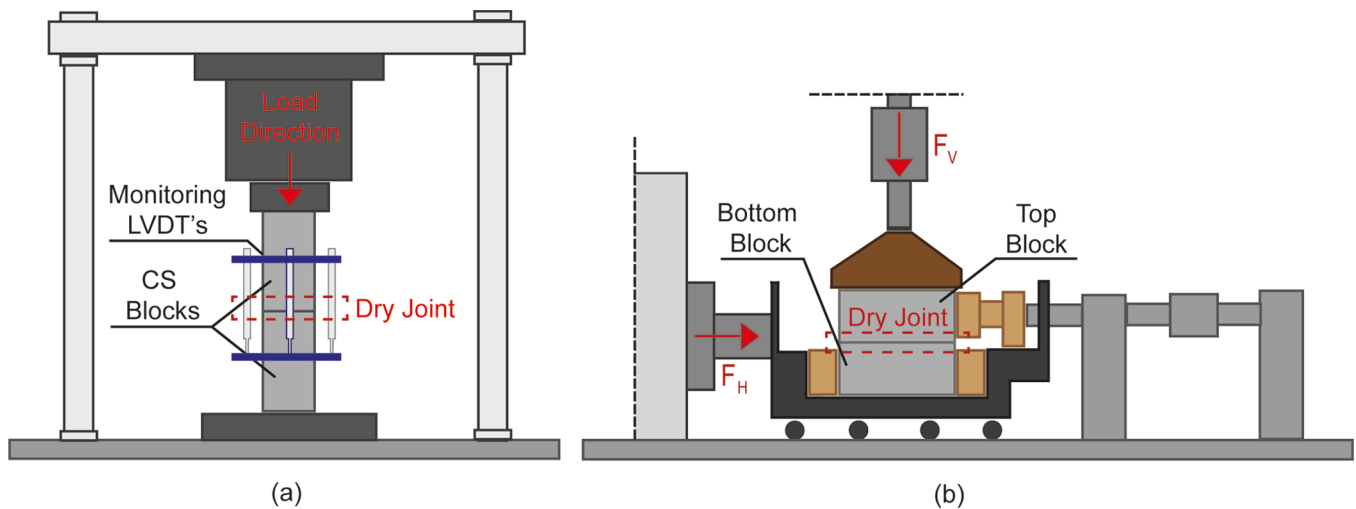


Fig. 1. Experimental setup sketches: (a) normal joint stiffness evaluation by means of joint closure tests and (b) tangential joint stiffness evaluation through direct shear box tests.

was also applied in [11,12], which included the actual value of the frictional resistance defined as a weighted value dependent on the crack line angle. In accordance with post-earthquake surveys, these models also account for openings, which are a significant factor of weakness for this mechanism [10].

Recently, LA of masonry corners was also used as the first step of a workflow to identify the most likely collapsing macroblock's geometry [13]. The second step consisted of a simplified analytical dynamic rocking analysis of the identified macroblock [13]. Such an approach leads to an overall efficient and engineering-oriented tool, similar to what has also been proposed for masonry façades [14]. However, while most studies focused on the rocking-sliding mechanism of masonry corners, the experimental tests presented by [15] evidenced through tilting tests that a flexural mechanism can also develop. Consequently, a separate LA formulation for this flexural mechanism was proposed and calibrated against experimental results [15]. Nevertheless, the failure of corners was only investigated when loaded symmetrically with respect to both walls (i.e. $\pi/4$), thereby revealing a gap in the literature.

In general, LA-based tools neglect the structure's global behaviour and only focus on assessing pre-defined local failure mechanisms [3,5,7]. Nonetheless, in many cases, there is a need to investigate the non-linear global behaviour of masonry structures in more detail, and this may be achieved by adopting sophisticated numerical methodologies, such as the Finite Element Method (FEM) [16–19] or the Discrete Element Method (DEM) [20–24]. Such approaches model masonry using different representation scales: equivalent continuum, macroblocks, or discrete representations (i.e. micro-modelling). DEM, in particular, enables the explicit representation of the units and joints [21,25], thereby making it well-suited for modelling the response of blocky masonry structures. DEM has been applied with success to the analysis of both unreinforced and retrofitted, dry-joint and mortared, masonry wall assemblies [22,24,26–33]. Despite the accuracy, the computational efficiency of the available numerical methods is rarely compatible with the need to have a rigorous real-time post-earthquake assessment [34]. Thus, researchers are committed to developing alternative modelling approaches and practical tools to decrease the computational cost without compromising the accuracy [35–38].

As far as masonry built cultural heritage is concerned, joint behaviour can broadly be akin to dry-joint behaviour. Indeed, if present, it is common that mortar deteriorated through time losing its bonding properties. Therefore, this paper focuses on dry-joint masonry specimens. Single-leaf and scaled (1:4) masonry corners tested on a tilting table are adopted as they provide a relatively simple validation

framework for numerical and analytical models. The objectives of the present work are summarised below:

- Provide experimental data to validate numerical and analytical methodologies to study the stability of masonry corners.
- Provide an illustrative example of the complete characterisation of dry-joint masonry specimens at low normal stress, including dry-joint stiffness.
- Quantify the effect of the seismic orientation on the failure mechanism and associated collapse load multiplier of masonry corners.
- Improve existing analytical LA models to account for the orientation of the seismic loading in an integrated way.
- Validate LA predictions of the collapse load multiplier and failure mechanism against experimental and numerical DEM results.

The experiments are reproduced numerically using the Discrete Element software 3DEC, while a novel analytical LA formulation for masonry corners is also developed. Such a general formulation allows to consider, jointly or separately, rocking-sliding and flexural mechanisms noted by [15] and accounts for the orientation of the seismic loading.

In short, this work investigates the influence of the orientation of the seismic load (adopting static lateral loading) on the capacity and failure mechanism of dry-joint masonry corners. The paper is organised as follows. Section 2 describes in detail the experimental campaign that concerns the mechanical characterisation of both the blocks and interfaces and the tilting tests of the masonry corner prototypes. Section 3 is devoted to the DEM model and its validation against the experimental results. Experimental and numerical observations are subsequently adopted to formulate a new analytical formulation based on LA in Section 4. Finally, relevant conclusions are drawn in Section 5.

2. Experimental campaign

In this section, the experiments involving single-leaf dry-joint masonry corners are presented. The campaign studies the influence of the seismic loading direction on masonry connections and constitutes a reference for validating analytical and numerical results. Furthermore, the investigation describes the characterisation of the material, including unit and interface properties.

2.1. Material characterisation

The masonry corners were built of dry calcium silicate (CS) blocks,

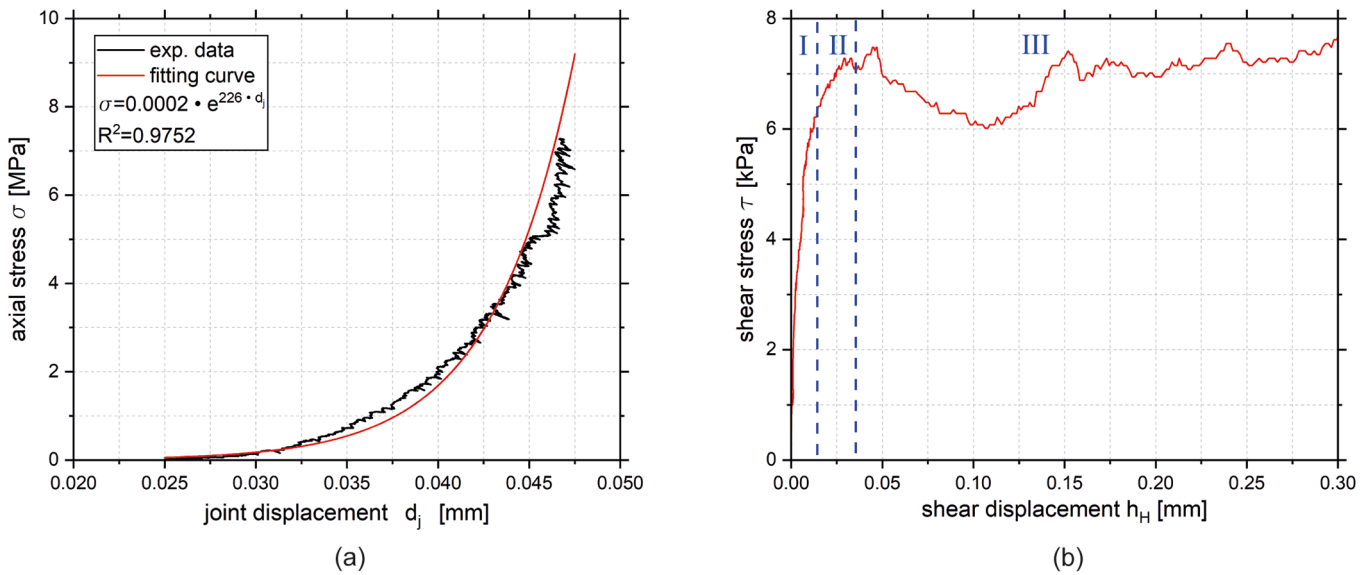


Fig. 2. (a) Fitting process to evaluate the stress dependency of joint normal stiffness and (b) example of the stress-displacement curve obtained from direct shear tests.

provided by the Xella Company [39], which were sawn to dimensions $t \times l \times h = 57.3 \pm 0.6$ (1.1%) \times 114.9 ± 0.5 (0.5%) \times 70.3 ± 0.2 (0.3%) mm^3 and density equal to $\rho = 1876 \pm 17$ (0.9%) $\text{kg}\cdot\text{m}^{-3}$. Here, the standard deviation and coefficient of variation (CoV) are also given. The compressive strength f_{cr} of the units was evaluated, following the ASTM D 2938-95 [40] standard, through five uniaxial displacement-controlled compression tests on prismatic bricks. The tests provided a value equal to $f_{cr} = 36.5 \pm 2.4$ (6.6%) MPa. The Young's modulus was subsequently obtained through ten compression tests along the three orthogonal material directions [41]. Besides a small anisotropy due to the industrial vibro-compaction production process, a value of 7.0 ± 1.16 (16.5%) GPa was found to characterise the material.

Joint normal k_n and shear k_s stiffnesses describe the variation of the normal (or shear) stress with the normal (or shear) displacement. They constitute critical numerical parameters in discrete element modelling approaches, though no clear guidelines already exist to support their identification. Herein, the normal joint stiffness k_n was characterised through classical joint closure tests [42–46], which consisted of uniaxial compression tests on two-stacked CS blocks (Fig. 1a). The displacement reading was obtained using four monitoring LVDTs placed around the blocks in the vicinity of the dry-joint, supported by two aluminium rings bounding the extremity. The tests were displacement-controlled through an additional LVDT measuring the actuator movement and consisted of five loading-unloading cycles. At the beginning of each loading cycle, the joint was completely unloaded to obtain stress-displacement relationships for very low stresses, here up to 0.01 MPa. Fig. 2a shows an example of the obtained experimental curves, in which the displacement due to block elastic deformation has already been removed based on the previously evaluated Young's modulus. After an initial phase of joint closure, where relatively low stresses trigger large displacements, the slope (i.e. the joint stiffness) dramatically increases for larger stress levels. Each experimental curve has been fitted using an exponential function (Fig. 2a), which expresses the stress as a function of the joint closure d_j and two empirical constants A and B as follows [42]:

$$\sigma = A \times e^{B \times d_j} \quad (1)$$

Differentiating both sides of Eq. (1) with respect to the normal joint displacement d_j , the normal joint stiffness reads:

$$k_n = \frac{d\sigma}{dd_j} = B \times \sigma \quad (2)$$

From the 25 tests conducted, two outliers have been disregarded, and the mean value of the empirical constant B was found equal to $B = 195.6 \pm 49.4$ (25.3%) mm^{-1} . It is noted that the coefficient of variation of this joint property is much larger than the ones found for the mechanical properties of the unit (6.6% for compressive strength and 16.5% for Young's modulus). This difference is explained by the larger variability of the physical properties of the joint (e.g. surface's roughness, geometrical tolerance) which directly influence the joint stiffness compared to volumetric properties.

Direct shear tests were also conducted to evaluate the tangential stiffness k_s of the dry-joints. The specimens consisted of two CS blocks of 55.82 ± 1.17 (2.1%) mm length, 57.65 ± 0.27 (0.5%) mm width and 27.15 ± 0.81 (3.0%) mm height. The test setup was composed of i) a bottom block located within the box base and pushed by a horizontal force F_H and ii) a fixed top block subjected to a constant normal force F_V (Fig. 1b). The data acquisition system comprised two load cells measuring the vertical and horizontal forces F_V and F_H , while the relative normal and shear displacement between the bottom and the top blocks was monitored by a Digital Image Correlation (DIC) system, which has already been employed in the literature for extracting the interface stiffness, proving its efficiency against other types of acquisitions [47]. This non-contact full-field measurement method solely identifies the relative displacement between the two blocks, whereas the shear box displacement acquisition system, i.e. vertical and horizontal LVDTs, also measures the external compliances owing to the shear box rig.

Fig. 2b provides an example of the obtained shear stress-displacement curve assuming a pre-compression of 10 kPa. The first window (I) corresponds to the so-called “elastic-stick” regime, in which the increase of shear stress leads to very small relative displacements [47,48]. In the second window (II), micro-slips progressively develop: at the micro-scale, some asperities are in adhesion (i.e. stuck), while other asperities experience relative tangential displacements. Such a phase is a transition from window I to window III, which corresponds to the gross slip phase, where all the asperities experience relative tangential displacement: the value of shear stress reaches the shear strength of the joint. Ten tests were carried out and no dilatancy has been noticed, similar to [49].

The tangential stiffness k_s was estimated by considering the slope of the elastic-stick phase (I), where the stress grows with a linear trend with respect to the displacement. Since the vertical stresses involved in the

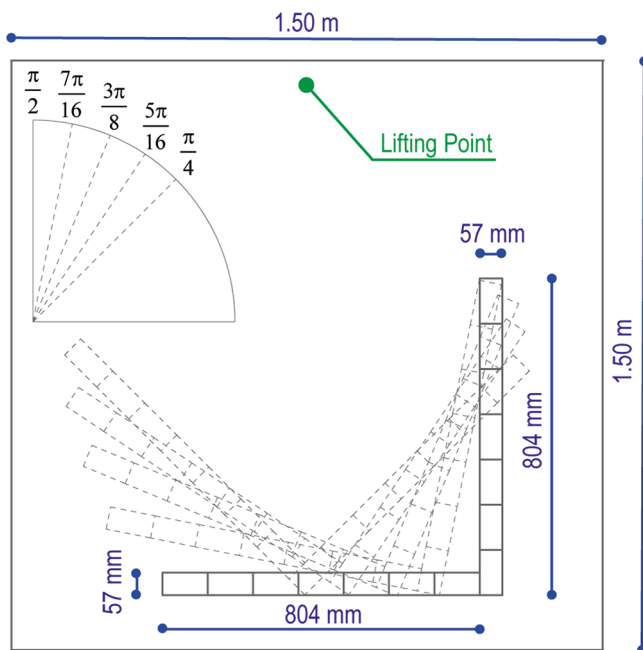


Fig. 3. Top view sketch of the corner position by varying the bisector direction.

experiments lie between 0 kPa and 10 kPa, the shear tests assumed 5 kPa and 10 kPa for the vertical stresses. Five tests for each pre-compression level were performed, obtaining a mean value of $k_s = 0.33 \pm 0.07$ (22.8%) $\text{GPa}\cdot\text{m}^{-1}$ at 5 kPa and $k_s = 0.49 \pm 0.25$ (51.1%) $\text{GPa}\cdot\text{m}^{-1}$ at 10 kPa. Again, a high coefficient of variation is obtained for the interface stiffness. Moreover, it is noted that the ratio between shear and normal stiffness for these two levels, using the previous expression for the normal stiffness, is 0.34 and 0.25, which is also in line with results found by others [50,51].

Finally, the shear (III) strength was extracted from the shear box tests considering 11 normal loading conditions, i.e. from 3 kPa to 50 kPa [52]. Assuming a Coulomb behaviour for the joint, the friction coefficient was estimated through linear regression of all the experimental outcomes and results in $\mu = 0.67$ ($R^2 = 0.97$).

The material characterisation process was completed by identifying the friction coefficient also through pseudo-static tilting tests, which was then compared with the results from the direct shear tests. Two bottom blocks were fixed to the tilting table, while a top unit was left free to slide. The table was then progressively inclined to obtain the block-block friction coefficient, while a digital inclinometer attached to the table allowed the reading of the sliding angle. A total of 50 tests were per-

formed, leading to a mean value of $\mu = 0.66 \pm 0.06$ (9.5%), with a range between 0.50 and 0.78. This value is close to the one identified through direct shear tests, especially when considering the experimental scatter. The obtained variability can be related to the surface's dustiness and also to some geometrical effects due to the presence of two interfaces instead of one. The mean value $\mu = 0.66$ is hereafter assumed globally representative of the dry-joint behaviour of the CS blocks, given the agreement with the shear box tests and the fact that this testing condition (i.e. layout of the joint) is physically closer to the corner's test setup.

2.2. Test setup

Tilting table tests have often been adopted as a tool to study collapse mechanisms of masonry structures [15,53,54]. A simple apparatus approximates the seismic forces through the progressive tilting of one extremity of the table: seismic forces are experimentally represented as static horizontal actions proportional to the specimen mass. Despite their simplicity, tilting tests estimate the horizontal collapse load multipliers of given structures and make it possible to observe the associated failure mechanisms [54].

The present experimental campaign focuses on studying the capacity of masonry corners to withstand horizontal forces with respect to seismic load orientation. Experimentally, the building-up process varied the direction of the corner bisector plan towards the rotational axis of the hinge (Fig. 3). More in detail, five load orientations equally spaced by $\pi/16$ were analysed, i.e. $\pi/4$, $5\pi/16$, $3\pi/8$, $7\pi/16$ and $\pi/2$. The specimen consisted of a single-leaf dry-joint masonry corner, which comprised two walls of, ideally, 804 mm in length and 633 mm in height (Fig. 3 and Fig. 4). The courses had seven full blocks for each wall, staggering the joints between the layers and reaching nine horizontal courses (Fig. 4a).

A total of 25 tests (5 per configuration) were performed at the laboratory of the University of Minho in Guimarães (Portugal). The adopted testing rig consisted of a $1.5 \text{ m} \times 1.5 \text{ m}$ steel table welded on a double T frame. The table was connected to an actuator through a steel wire that allows the uplifting of one extremity, while the other end rotated around a hinge [56]. Tilting speed was set to $0.1^\circ\cdot\text{s}^{-1}$ before an angle of 9° and $0.02^\circ\cdot\text{s}^{-1}$ afterwards, in order to ensure quasi-static conditions close to the specimen collapse.

Sliding between the first course and the steel table was prevented by fixing this course to the table with a double-faced tape, while the uprightness and repeatability of the building up process were ensured using a timber guiding system. The free ends of the walls were clamped with an L-shaped profile and rubber pads to simulate ideal boundary conditions (Fig. 4b).

A digital inclinometer installed on the table captured the rotation angle, while the collapse mechanism was recorded by two digital cam-

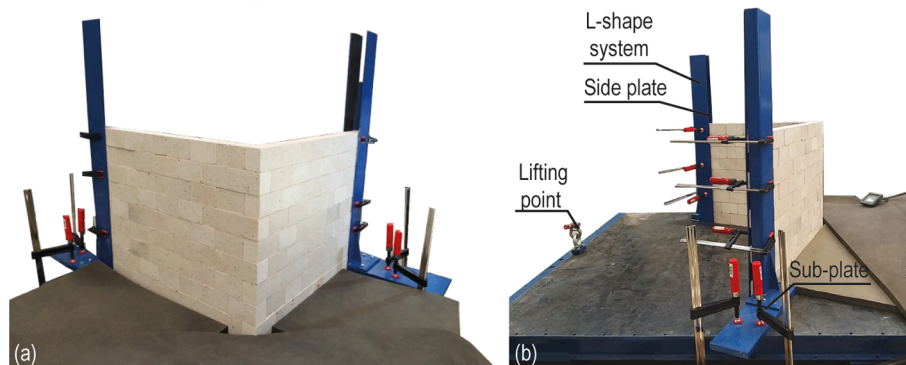


Fig. 4. (a) Corner $5\pi/16$ test setup and (b) side view of the clamping system.

Table 1
Experimental results, load multiplier λ_α .

Load orientation α	Load Multiplier λ_α	
	Mean Value λ	CoV [%]
$\pi/4$	0.287	2.0
$5\pi/16$	0.270	3.9
$3\pi/8$	0.248	3.0
$7\pi/16$	0.239	1.3
$\pi/2$	0.236	3.6

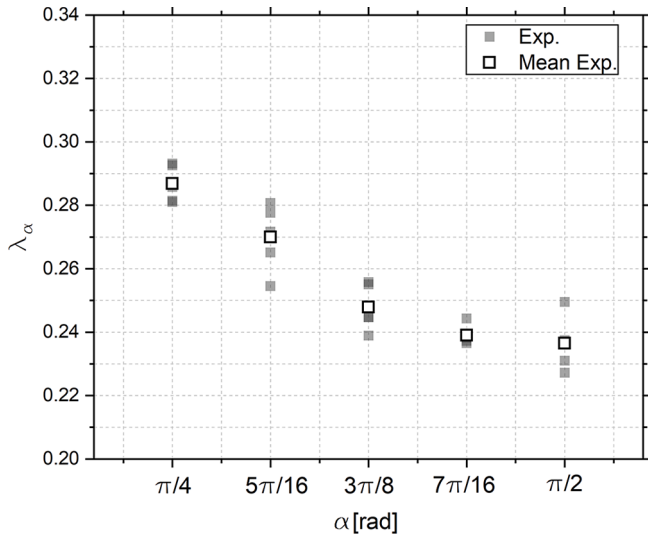


Fig. 5. Experimental load collapse multiplier λ_α obtained for all the orientations tested.

eras placed orthogonally to the plane of each sidewall. Finally, three lights were installed in the vicinity of the corner to allow a recording speed of 10 Hz with a shutter speed of 4 ms.

2.3. Experimental results

In this section, the outcomes obtained from the experimental campaign are presented. The results in terms of load multiplier (i.e. ratio between horizontal and vertical loading) λ_α are listed in Table 1, while full details of the experimental dataset are publicly available in [55]. As stated, the repeatability and reliability of the results were ensured by including five tests for each direction (the CoV is very small, demonstrating the low scatter). Additionally, similar collapse mechanisms have been found for tests belonging to the same group.

As Fig. 5 illustrates, the collapse load multiplier decreases following a non-linear trend from $\pi/4$ to $\pi/2$. It can be observed that the highest capacity of the system is obtained when the load direction is coincident with the corner bisector, i.e. $\pi/4$, resulting in an increase in the capacity by 21% compared to the $\pi/2$ case. Indeed, when rotating the corner towards the $\pi/4$ orientation, the out-of-plane component acting on each wall is reduced. Additionally, the different types of failure mechanisms, namely rocking, sliding and horizontal flexural, depend on the orientation of the corner.

The collapse mechanism for the loading conditions $\pi/4$, $5\pi/16$, $3\pi/8$, $7\pi/16$ and $\pi/2$ are depicted in Fig. 6. The configurations for which the load is applied in the direction of the bisector, i.e. $\pi/4$ (Fig. 6a), develop a mixed mechanism that comprises both in-plane and out-of-plane components in each wall. Both walls show a predominant out-of-plane component, appearing at first with an out-of-plane sliding of the units. This initial phase is then followed by an uplift of the blocks

that contributes to the formation of three cylindrical hinges in both walls: i) the first one is located in the vicinity of the boundary conditions, i.e. line O'A' and line O''A'', and appears fully open, ii) the second one is fully formed and shows up in a central wall area corresponding to the inner wall side, i.e. line O'B' and line O''B'', iii) the third one develops in an area close to the wall intersection and it is only triggered in the left wall, line O'C', and completely open in the right wall, line O''C''. Fig. 6b displays the collapse mechanism of the $5\pi/16$ case. In this configuration, the left wall shows a similar mechanism to the $\pi/4$ case, while the right wall presents a higher displacement in-plane, followed by an out-of-plane mechanism. Similar collapse mechanisms have been registered for $3\pi/8$ (Fig. 6c), $7\pi/16$ (Fig. 6d) cases and the weakest condition, namely $\pi/2$ (Fig. 6e). The right wall works in its plane, showing a clear initial sliding phase of the units followed by a rotation around O'' (Fig. 6c, d, e-right). At the same time, the orthogonal wall experiences a predominant out-of-plane mechanism, which results in the creation of two macroblocks, namely O'A'B' and O'B'C' (Fig. 6c, d, e-left). It is worth noting that the macroblock O'A'B' is formed thanks to two cylindrical hinges fully formed, i.e. O'A' and O'B', while the onset of the O'C' is triggered but not fully formed. In particular, the cylindrical hinge O'C' dissipates a minimal amount of energy, resulting in pseudo orthogonality between the two walls in the kinematic collapse configuration.

3. Numerical (DEM) modelling

Numerical analyses of the corner specimens have been conducted using DEM in 3DEC [57]. In this section, the model setup is first briefly presented, following which its predictions are validated against the experimental results.

3.1. Model setup

Using DEM, the individual units making up a structure can be modelled as either rigid or deformable blocks. In the latter case, the blocks are discretised using a finite element mesh. In the present work, the specimens are modelled as an assembly of rigid blocks, as these are more suitable for quasi-static analyses [57]. All the system deformability is therefore concentrated in the joints and each block is characterised by the experimental density of $1876 \text{ kg}\cdot\text{m}^{-3}$ and 6 degrees of freedom.

Interaction between the blocks is modelled using zero-thickness non-linear springs (point contacts), which are automatically created when two block faces are determined to be in contact. The point contacts approach allows the modelling of large displacements and complete separation between blocks, which makes it particularly suitable for problems of stability and/or collapse. In the case of rigid blocks (as used herein), point contacts (sub-contacts) are generated through triangulation of the block faces and are usually created at each block face's vertices [57]. By default, rectangular block faces are divided into two triangles, resulting in four-point contacts (Fig. 7); however, more contact points are usually required to capture the contact stress distribution accurately [21]. In this study, the triangulation density is increased so that each block comprises 10, 7 and 6 contact points along its length, height, and thickness, respectively. Using the contact points approach, the resultant force increment ΔF at each contact point can be determined through the relative incremental displacement Δu between the blocks at that point, the contact spring stiffness k , as well as the sub-contact area A_c . The latter is typically equal to 1/3 of the areas of the triangles containing the contact point (Fig. 7).

As a soft contact approach is used here, the extent of interpenetration between blocks is controlled by the stiffness of the springs. Though Section 2.1 evidenced the dependency of stiffness on axial stress, in this work, stiffness is considered homogeneous and is taken equal to the average value in the specimens, as given next. From the geometry and density of the specimens, the axial stress at mid-height of the specimen is $\sigma = (0.633 \times 1.876 \times 9.81)/2 = 5.82 \text{ kPa}$. According to Eq. (2), the

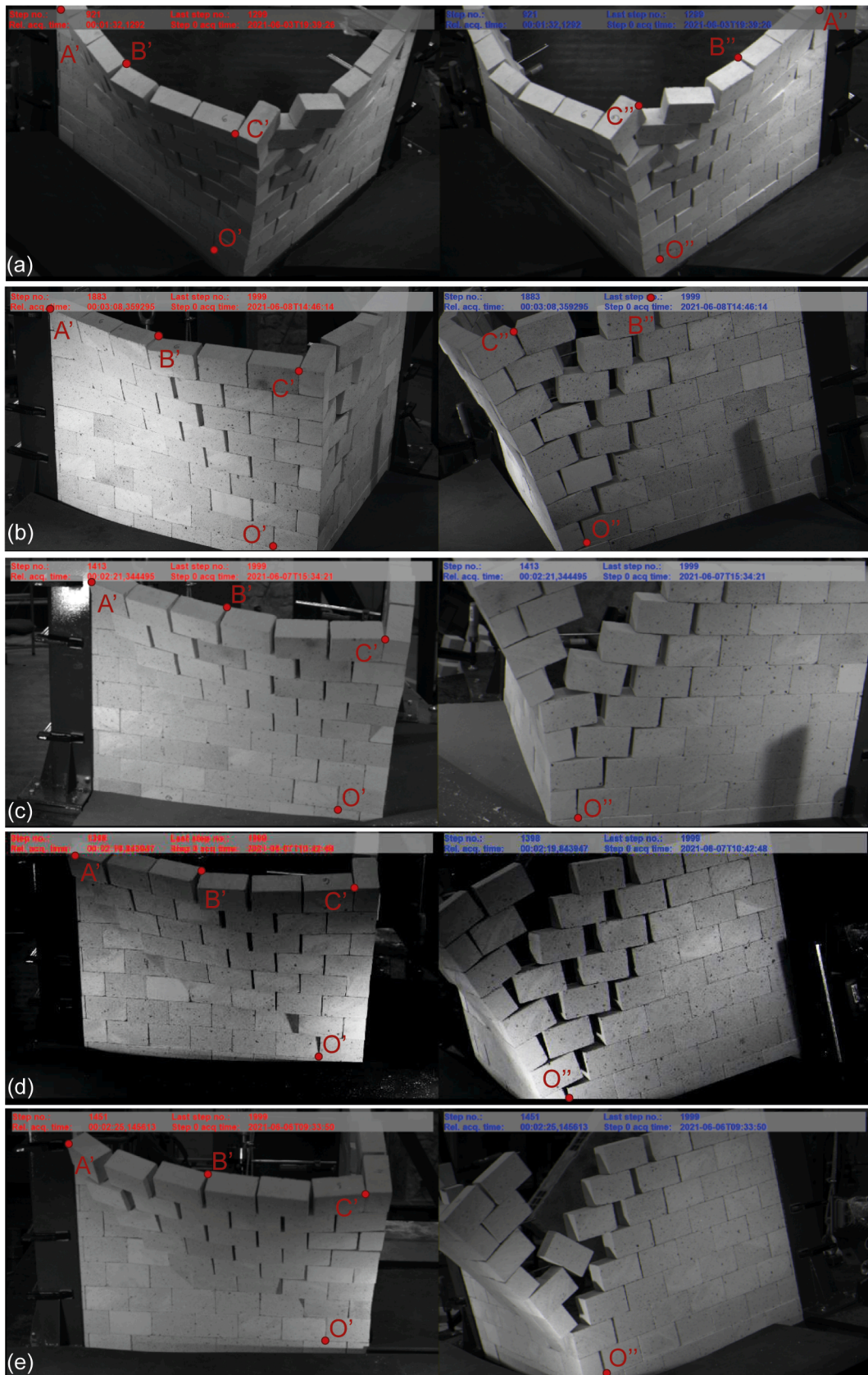


Fig. 6. Failure mechanisms for (a) Corner $\pi/4$, (b) Corner $5\pi/16$, (c) Corner $3\pi/8$, (d) Corner $7\pi/16$ and (e) Corner $\pi/2$.

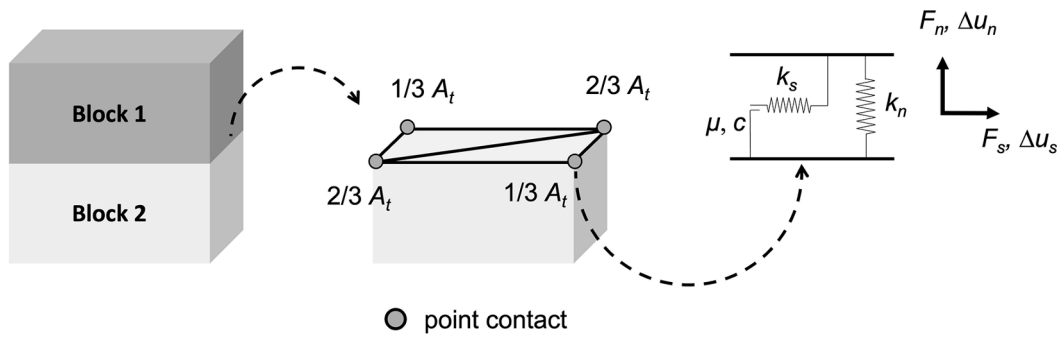


Fig. 7. Mechanical representation of contact between blocks.

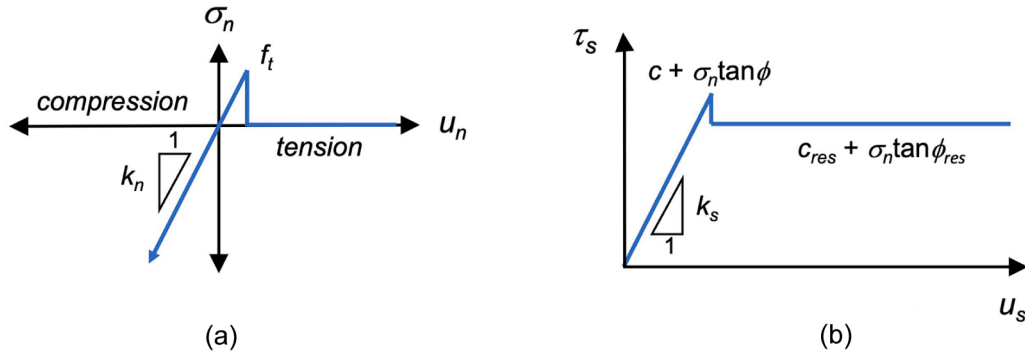


Fig. 8. Coulomb friction joint (a) normal stress versus normal displacement and (b) shear stress versus shear displacement behaviour (adapted from [57]).

average normal stiffness of the dry-joints therefore equals $k_n = 195.6 \times \sigma = 1.14 \text{ GPa}\cdot\text{m}^{-1}$. Similarly, the tangential stiffness is determined to be $k_s = 0.33 \text{ GPa}\cdot\text{m}^{-1}$. The non-linear response of the point contacts is controlled via the tensile strength f_t in the normal direction and the Coulomb-slip joint model in the shear direction (Fig. 8), which consequently depends on the values specified for the cohesion c and friction coefficient μ (indicated by $\mu = \tan\phi$ in Fig. 8). Herein, null values are selected for the tensile strength and the cohesion of the dry-joints, while the dilatancy angle ψ is set to zero, according to the direct shear tests (Section 2.1) and literature [49]. On the other hand, the friction coefficient is set to the value of $\mu = 0.66$ ($\phi = 34^\circ$) obtained through the tilting tests.

With respect to the boundary conditions, the blocks at the end of the walls are fixed to reproduce the clamped conditions of the experiment. Similarly, the bottom course is fixed in order to model the effect of the double-faced tape (see Fig. 9, shown here for the $\pi/4$ corner test setup).

In terms of loading, to simulate the tilting table, the vertical component of gravity is kept constant at $10 \text{ m}\cdot\text{s}^{-2}$, while the horizontal component is progressively increased in steps of $0.05 \text{ m}\cdot\text{s}^{-2}$. For each load increment, the analysis is run until the maximum velocity in the system is less than $0.001 \text{ m}\cdot\text{s}^{-1}$, and only once the convergence criterion is satisfied is the loading increased. Failure is considered to occur with a lack of convergence of the maximum velocity, and the simulations are continued until the maximum displacement of the system exceeds 0.7 m , to obtain the complete collapse of the structure.

The equations of motion of the system are solved by means of an explicit time-stepping scheme, which makes use of a central-difference algorithm [21]. At each timestep, the relative velocity across a sub-contact (contact point) is first determined and then converted into a relative incremental displacement Δu . This displacement is resolved into its normal and shear components, Δu_n and Δu_s , and is consequently used to determine the force increments. The total normal and shear forces for the sub-contacts are subsequently updated and adjusted based on the contact constitutive relations (in this case, the Coulomb-slip joint

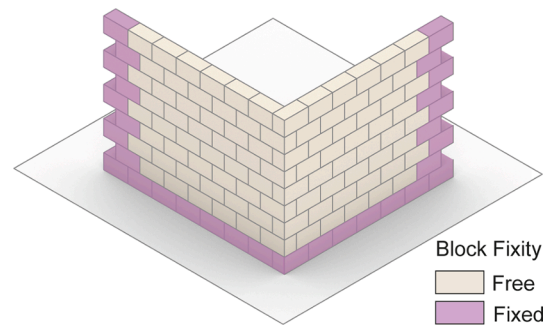


Fig. 9. Final 3DEC model.

model). The sub-contact forces are added to the forces/moments acting on the relevant block centroids, and the corresponding equations of motion are then integrated to obtain the new block velocities and positions, which serve as input for the next calculation cycle. Note that to ensure numerical stability, a suitably small timestep is required for the analyses, which is automatically calculated by the program and is directly proportional to the smallest nodal mass and inversely proportional to the maximum contact stiffness of the system. Consequently, a decrease in nodal mass tends to increase the overall solve time (e.g. more contact points, resulting from an increase in the triangulation density).

For static and pseudo-static solutions, the equations of motion are damped in such a way that they reach a force equilibrium state as rapidly as possible. Conceptually similar to dynamic relaxation, a damping force, proportional to the velocity of the blocks, is artificially added into the equations of motion to avoid oscillations around the equilibrium position [57]. Here, local damping with the default value of 0.8 is used, whereby an additional/artificial damping force is applied on each node. This force is proportional to the magnitude of the unbalanced force at that same node, in a direction such that energy is always dissipated [57]. This form of damping is usually recommended for

Table 2
Comparison of the experimental and numerical load multipliers λ_α , with Difference (%) = $(\lambda_\alpha^{NUM} - \lambda_\alpha^{EXP})/\lambda_\alpha^{EXP} \times 100$.

Load orientation α	Load Multiplier λ_α		Difference (%)
	Experimental	Numerical	
$\pi/4$	0.287	0.315	9.8
$5\pi/16$	0.270	0.290	7.4
$3\pi/8$	0.248	0.270	8.9
$7\pi/16$	0.239	0.265	10.9
$\pi/2$	0.236	0.270	14.4

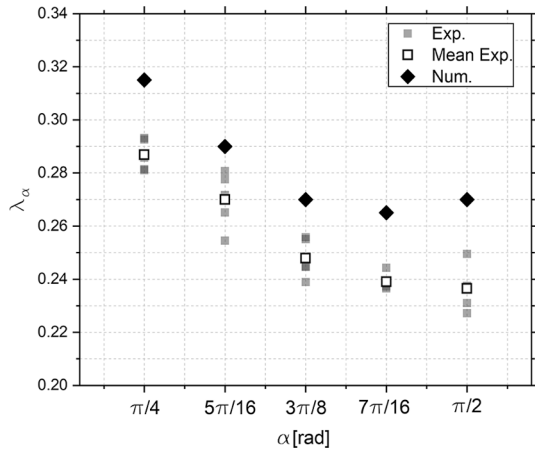


Fig. 10. Variation of collapse load multiplier with load orientation for both the experimental tests and numerical models.

static/pseudo-static analyses and can minimise oscillations arising from abrupt failure of the model [22,57].

3.2. Experimental validation

The results of the numerical models have been evaluated in terms of the load multipliers λ_α and associated collapse mechanisms obtained for each load orientation angle α . In terms of the collapse load multipliers, as Table 2 and Fig. 10 indicate, the predictions of the numerical model

generally tend to follow the same trend as the experiments, with the load multiplier globally decreasing in a non-linear manner from $\pi/4$ to $\pi/2$. However, the numerical model appears to consistently overestimate λ_α , with an average overprediction of about 10%.

This slight overestimation is likely to be partly due to the fixed boundary conditions assumed in the numerical model, which do not permit any rotations and consequently increase the stiffness of the walls in the out-of-plane (OOP) direction. The effect of this assumption increases as the OOP load component acting on the individual walls grows and explains why, in the case of the $\pi/2$ orientation, where one of the walls is loaded entirely in the OOP direction, a higher load multiplier is required to cause a local collapse.

In addition to the effect of the boundary conditions mentioned above, the overestimation of the load multiplier is also attributed to other assumptions of the numerical model, such as perfect (zero-thickness) joints between blocks and uniform cross-sections within the blocks. This first assumption is most likely not the case in reality for the vertical (head) joints, where small gaps between the blocks could decrease the in-plane and flexural capacities of the walls. Additionally, given that the CS blocks used in the experiments have been manually sawn, it is unlikely that they would have perfectly uniform cross-sections.

Given that the walls are already quite slender in the out-of-plane (OOP) direction ($H/t = 10$), small differences in the thickness of the blocks (decrease of a few mm) may increase the overall slenderness and therefore decrease the capacity of the wall in the out-of-plane direction as well. Thus, two sets of additional numerical simulations have been run with a reduced thickness (increased slenderness). The first uses a 5% reduction in thickness (and therefore an approximately 5% increase in slenderness), while the second uses a 10% reduction in thickness (or conversely a 10% increase in slenderness). Note that a thickness reduction higher than 10% (i.e. 5.7 mm) was not considered reasonable given the near-perfect edges of the CS blocks.

The results of these analyses can be found in Fig. 11a and Table 3, where it can be seen that although an increase in slenderness does cause a slight decrease in the collapse load multiplier, the numerical simulations still overestimate λ_α , with an average overprediction of 8% and 6% for the 5% and 10% thickness reduction cases respectively. Thus, the non-uniform cross-sections of the CS blocks are unlikely to be a significant cause of the discrepancy between the numerical and experimental results.

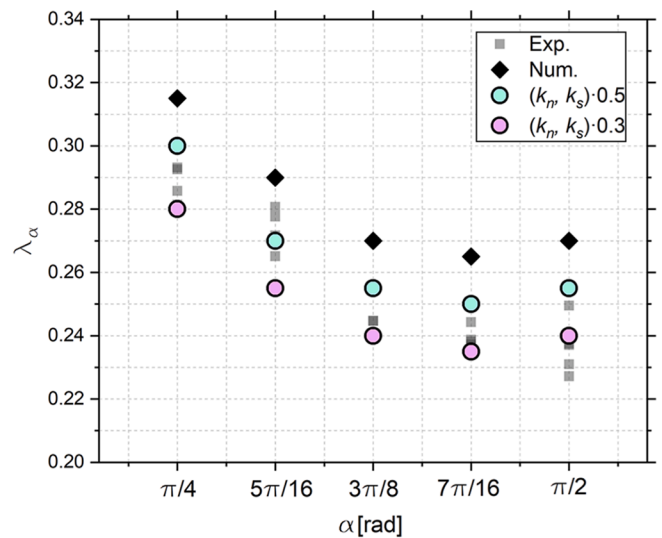
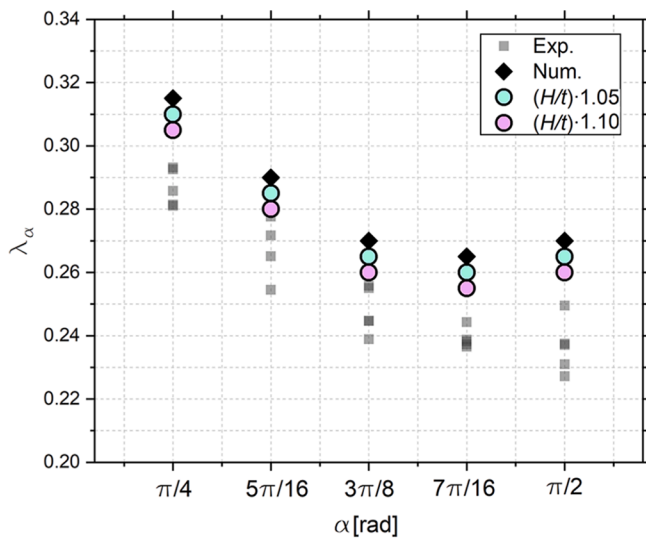


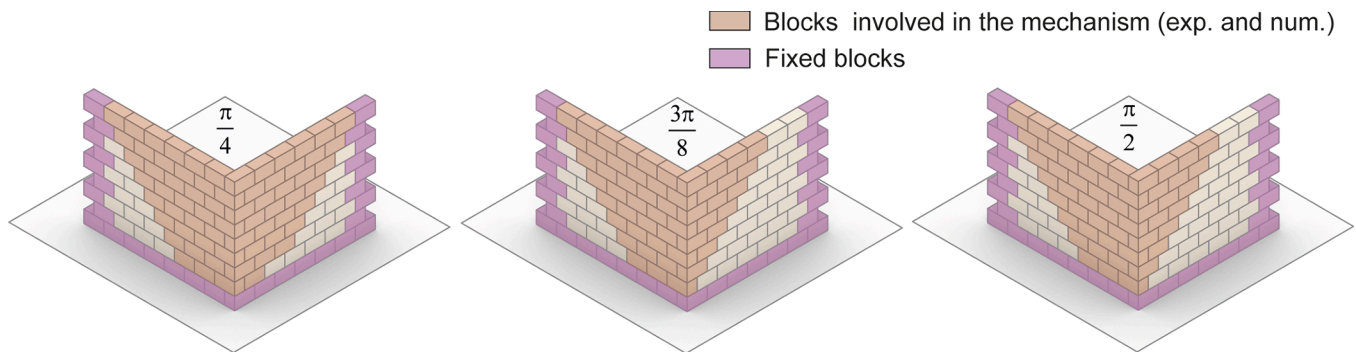
Fig. 11. Variation of collapse load multiplier with load orientation for both the experimental tests and numerical models, for (a) different slenderness (H/t) ratios and (b) different stiffnesses (k_n, k_s).

Table 3Comparison of experimental and numerical load multipliers λ_α for different slenderness (H/t) ratios, with Difference (%) = $(\lambda_\alpha^{NUM} - \lambda_\alpha^{EXP})/\lambda_\alpha^{EXP} \times 100$.

Load Multiplier λ_α					
Load orientation α	Experimental	Numerical (H/t)-1.05	Difference (%)	Numerical (H/t)-1.10	Difference (%)
$\pi/4$	0.287	0.310	8.0	0.305	6.3
$5\pi/16$	0.270	0.285	5.6	0.280	3.7
$3\pi/8$	0.248	0.265	6.9	0.260	4.8
$7\pi/16$	0.239	0.260	8.8	0.255	6.7
$\pi/2$	0.236	0.265	12.3	0.260	10.2

Table 4Comparison of experimental and numerical load multipliers λ_α for different stiffnesses k_n and k_s , with Difference (%) = $(\lambda_\alpha^{NUM} - \lambda_\alpha^{EXP})/\lambda_\alpha^{EXP} \times 100$.

Load Multiplier λ_α					
Load orientation α	Experimental	Numerical (k_n, k_s)-0.5	Difference (%)	Numerical (k_n, k_s)-0.3	Difference (%)
$\pi/4$	0.287	0.300	4.5	0.280	-2.4
$5\pi/16$	0.270	0.270	0.0	0.255	-5.6
$3\pi/8$	0.248	0.255	2.8	0.240	-3.2
$7\pi/16$	0.239	0.250	4.6	0.235	-1.7
$\pi/2$	0.236	0.255	8.1	0.240	1.7

**Fig. 12.** Comparison in terms of blocks involved in the collapse mechanisms for the experimental and numerical tests, for the different load orientations.

In fact, another source of discrepancy could be attributed to the values adopted for the joint normal stiffness k_n , which was herein evaluated through classical joint closure tests. In [44], the authors have demonstrated that the local normal stiffness of joints belonging to a staggered masonry wall is approximately 2 to 3 times lower than that evaluated through joint closure tests. This is due to the existence of misalignment and dimension differences between blocks in a wall, where contact is never only between two blocks (case of the joint closure tests). To that end, two additional sets of simulations have been conducted – the first one reducing the normal stiffness by a factor of 2 (or 50%) and the second reducing the normal stiffness by a factor of 3 (so to approximately 30% of the original stiffness). In the absence of similar information about the tangential stiffness k_s , it was chosen to keep the initial ratio of k_s/k_n constant for these analyses. The results of these additional analyses can be found in Fig. 11b and Table 4.

As Fig. 11b illustrates, the numerical models demonstrate a sensitivity to the joint stiffness. Decreasing this parameter by a factor of 2 causes a substantial decrease in the collapse load multiplier, with the numerical predictions now lying within the range of the experimental scatter, with an average overprediction of 4% (with respect to the mean experimental values). Similarly, reducing the joint stiffness by a factor of 3 further reduces the collapse load multiplier, with the numerical predictions now providing a lower bound to the experimental results and, on average, underpredicting λ_α by 3%. These analyses thus demonstrate the importance of evaluating the joint stiffness on the whole masonry wall, and not just through joint closure tests. Nevertheless, it is worth underlining that the sensitivity analyses investigate the variation of a single parameter individually (i.e. slenderness or stiffness), while most

likely the global outcome includes the influence of combined factors. For this reason, it is understood that the adopted range of stiffness variation may be reduced if concurrently considering other sources of uncertainties.

With respect to the collapse mechanisms, a near-perfect agreement has been found between the numerical models and the experiments in terms of the blocks involved in each mechanism (see Fig. 12). Note that as similar mechanisms were obtained from the four sets of parametric analyses, only the mechanisms from the original numerical analyses are presented here. A good agreement was also observed in terms of the shape of the failure mechanism and the associated hinge locations, as illustrated by Fig. 13, with the formation of horizontal flexural mechanisms in the out-of-plane loaded walls and rocking-sliding mechanisms in the in-plane walls. The two walls have also been observed to retain their orthogonality relative to each other. The main difference observed is in terms of the location of hinge B' on the OOP-loaded wall, which occurred one block closer to the corner in the numerical models, resulting in a slightly larger macroblock O'A'B' than the experimental tests for all considered load orientations.

4. Analytical model

The failure mechanism of the corner through an analytical model has been recently investigated by [15]. A three-dimensional macroblock model with frictional joints to analyse failure mechanisms was developed, with crack patterns and load factors derived through the kinematic approach of Limit Analysis (LA). This formulation considers either the rocking-sliding mechanism or the horizontal flexure phenomena

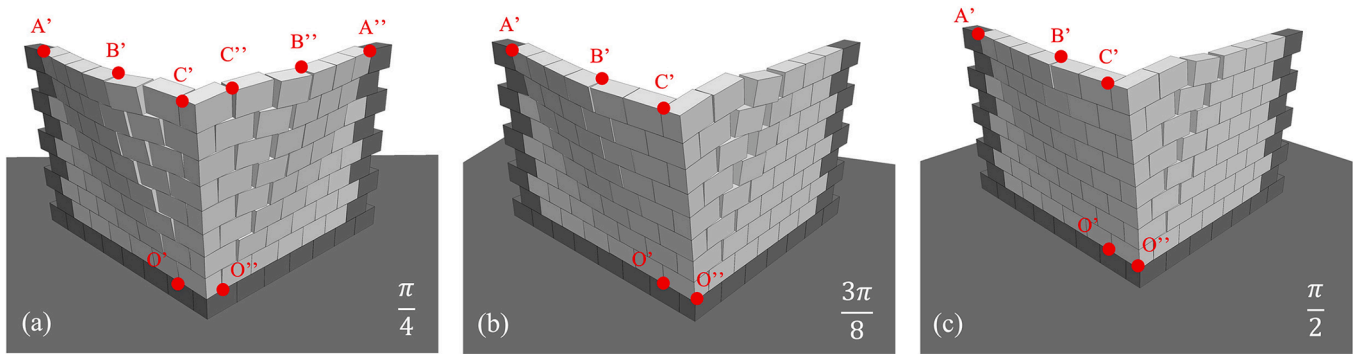


Fig. 13. Numerically-obtained failure mechanism configurations (hinge locations) of (a) Corner $\pi/4$, (b) Corner $3\pi/8$ and (c) Corner $\pi/2$ (see Fig. 6 for comparison).

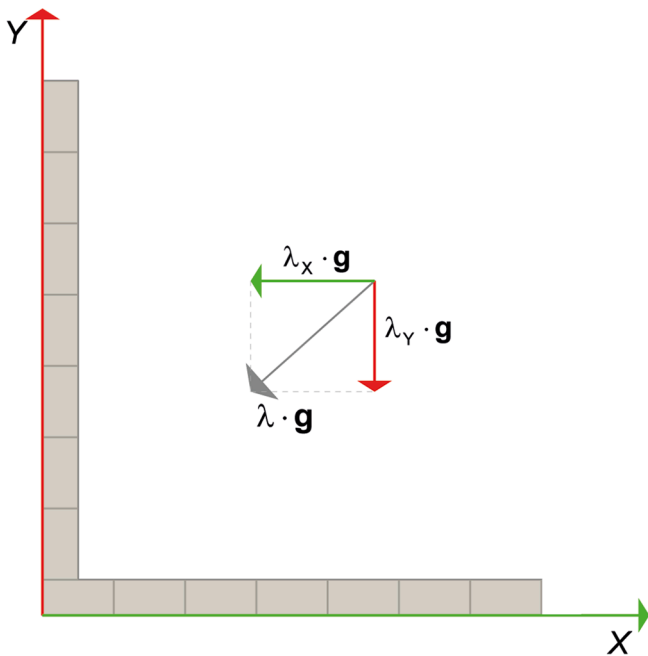


Fig. 14. Plan view of a masonry corner: horizontal action components along X and Y axes.

typically expected in masonry corners. Despite the good accuracy in terms of both horizontal multiplier and geometry of the failure mechanisms, such an analytical formulation presents limitations: i) the model cannot be applied when the masonry corner prototype is not symmetric, ii) the model is not able to predict the load multiplier and the geometry of the failure mechanism when the horizontal action is not passing from the bisector of the corner. Therefore, a new analytical model is proposed next.

4.1. Model formulation

The primary assumption in the analytical model is to decompose the horizontal action along with the X and Y directions (see Fig. 14). Thanks to this assumption, the mathematical formulation to compute the components λ_x and λ_y are fully uncoupled and hence may be treated separately. One can note that the horizontal cylindrical hinge is in turn considered perpendicular to the load actions, i.e. aligned with the X or Y axes.

Fig. 15 addresses the horizontal load component coincident with the X direction. It is required to mathematically describe the problem with the principle of virtual work and to represent the kinematics of the failure mechanism with only one virtual parameter: $\delta\theta$ (see Fig. 15). For this purpose, the following hypotheses arising from observations of the experimental campaign are adopted:

- Wall WX1 is assumed to collapse in its plane because of the rocking-sliding mechanism; this activates frictional resistance according to the formulation described in [35].

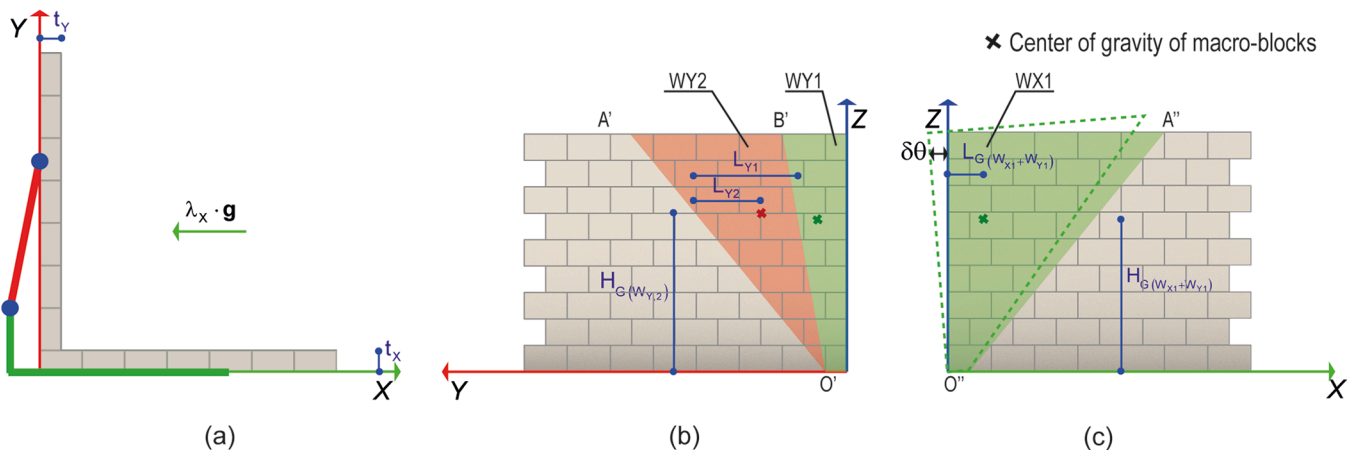


Fig. 15. Kinematic description of the failure mechanism: (a) plan view; (b) side view involving shear-torsion and rocking; (c) side view involving shear-rocking. $H_{G(WY2)}$, $H_{G(WX1 + WY1)}$, L_{Y1} , L_{Y2} and $L_{G(WX1 + WY1)}$ define the position of the centre of gravity of the red and green macroblocks. (For interpretation of the references to colour in this figure legend, the reader is referred to the web version of this article.)

- The two walls that compose the corner, i.e. WX1 and WY1, retain their orthogonality relative to each other (Sections 2.3 and 3.2). As shown in Fig. 6e, the macroblock O'B'C' rotates only slightly with respect to the macroblock of the second orthogonal wall that shows an in-plane rocking motion around O''. In short, the corner seems to keep the orthogonality since the cylindrical hinge O'C' can dissipate a lower amount of energy compared with O'A' and O'B'.
- Wall WY1 generates two cylindrical hinges, O'A' and O'B', which dissipate energy due to the shear-torsion interaction (see Fig. 15).

According to the adopted hypotheses, it is possible to draw the kinematic failure mechanism involving the corner prototype under a horizontal load acting along the X-direction (see Fig. 15). The mathematical formulation to calculate λ_X is based on the principle of virtual work, which requires the balance between the external and internal virtual works:

$$\delta W_{ext} = \delta W_{int} \tag{3}$$

The external virtual work contains the destabilising as well as the stabilising works performed by the inertial forces and is expressed as:

$$\delta W_{ext} = \lambda_X \cdot (W_{X1} + W_{Y1}) \cdot \delta_{O,X,1} + m \cdot \lambda_X \cdot W_{Y2} \cdot \delta_{O,X,2} + (1 - m) \cdot \lambda_X \cdot W_{Y2} \cdot \bar{\delta}_{O,X,2} - (W_{X1} + W_{Y1}) \cdot \delta_{R,X,1} - m \cdot W_{Y2} \cdot \delta_{R,X,2} - (1 - m) \cdot W_{Y2} \cdot \bar{\delta}_{R,X,2} \tag{4}$$

where, $\delta_{O,X}$ and $\delta_{R,X}$ are the virtual overturning and stabilising displacements of the centre of gravity of the macroblocks (index 1 and 2 indicate the green and red macroblocks, respectively), m assumes a value of 1 if the mechanism is affected by the horizontal flexural mechanism or 0 when the pure rocking-sliding mechanism is studied. When m is set to 0, it examines the failure mechanism composed of a unique rigid block, meaning that the hinge O'B' is not considered in the geometrical definition of the macroblocks (see Fig. 15). The virtual displacement contributions are a function of the virtual parameter $\delta\theta$, given by:

$$\begin{aligned} \delta_{O,X,1} &= \delta\theta \cdot H_{G(W_{X1} + W_{Y1})} \\ \delta_{R,X,1} &= \delta\theta \cdot L_{G(W_{X1} + W_{Y1})} \\ \delta_{O,X,2} &= \delta\theta \cdot H_{G(W_{Y2})} \cdot \frac{L_{Y2}}{L_{Y1}} \\ \bar{\delta}_{O,X,2} &= \delta\theta \cdot H_{G(W_{Y2})} \\ \delta_{R,X,2} &= \bar{\delta}_{R,X,2} = \delta\theta \cdot \frac{t_Y}{2} \end{aligned} \tag{5}$$

The second term of the Eq. (3) is the internal work that derives from the frictional forces along with line O''A'' and the shear-torsion interaction across the cylindrical hinges O'A' and O'B':

$$\delta W_{int} = \delta W_{int(shear)O''A''} + \delta W_{int(torsion/shear)O'A'} + \delta W_{int(torsion/shear)O'B'} \tag{6}$$

with:

$$\delta W_{int(shear)O''A''} = \delta\theta \cdot H_{i,X} \left(F_{max} \cdot \left(1 - \frac{\alpha_c}{\alpha_b} \right) \right)_{O''A''} \tag{7}$$

$$+ (1 - m) \cdot \delta\theta \cdot H_{i,Y} \left(F_{max} \cdot \left(1 - \frac{\alpha_c}{\alpha_b} \right) \right)_{O'A'}$$

$$\begin{aligned} &\delta W_{int(torsion/shear)O'A'} + \delta W_{int(torsion/shear)O'B'} \\ &= \delta\theta \cdot \frac{H_{G(W_{Y2})} \cdot L_{Y2} / L_{Y1}}{L_{Y2}} \cdot m \cdot k \cdot \left(T_0 \cdot \left(1 - \frac{F_{hinge,1}}{F_{max}} \right) + T_0 \cdot \left(1 - \frac{F_{hinge,2}}{F_{max}} \right) \right) \end{aligned} \tag{8}$$

where α_c and α_b are the actual crack inclination and the crack inclination upper threshold of the in-plane wall, respectively, k ($k \leq 1$) is introduced to reduce the contact surfaces caused by the uplift of the blocks along these hinges, $F_{hinge,1}$ and $F_{hinge,2}$ are the internal shear forces in equilibrium with the external forces at the hinges O'A' and

O'B', respectively. F_{max} is the maximum frictional force which is computed according to the formulation proposed by [58] and adopted in other studies [14]:

$$F_{max} = \left(\gamma \cdot v \cdot h \cdot t \cdot \frac{n \cdot (n + 1)}{2} \right) \cdot \mu \tag{9}$$

Here, μ is the friction coefficient, t is the block thickness, v is equal to $l/2$ and n is the number of unit courses. Referring to Eq. (7), at the cylindrical hinges O'A' and O'B', the frictional resistances develop via shear-torsion interaction. The yield function proposed in [15] has been adopted and the pure torsion T_0 is computed as:

$$T_0 = F_{max} \cdot d_0 \tag{10}$$

where d_0 is the torsion constant expressed by the relation:

$$d_0 = \frac{1}{12 \cdot t \cdot v} \left(v^3 \cdot \ln \left(\frac{t+d}{v} \right) + t^3 \cdot \ln \left(\frac{v+d}{t} \right) + 2 \cdot t \cdot v \cdot d \right) \tag{11}$$

where $v = \frac{l}{2}$ and $d = \sqrt{v^2 + t^2}$ [12].

Once the internal and external virtual works have been defined, it is possible to solve Eq. (3) for λ_X , which reduces to a polynomial function of all the geometrical variables involved in the problem.

Following the same approach, the horizontal load acting only along the Y direction λ_Y , is computed, but is not reported here for the sake of brevity. As explained earlier, the proposed approach aims to define the horizontal proportional gravity load multiplier considering any direction in the domain $\alpha \in [0, \pi/2]$. In this regard, the horizontal load multiplier can be expressed as a function of λ_X and λ_Y , which are then combined by means of two coefficients, namely A and B:

$$\lambda_\alpha = A(\alpha) \cdot \lambda_X + B(\alpha) \cdot \lambda_Y \tag{12}$$

Here, A and B assume the role of weight functions. In particular, A must be equal to 1 if $\alpha = 0$ and equal to 0 if $\alpha = \pi/2$. On the contrary, B must be equal to 0 if $\alpha = 0$ and equal to 1 if $\alpha = \pi/2$. One can note that for all the values of the domain $\alpha \in [0, \pi/2]$, the coefficients A and B may assume any possible value. However, a reasonable attempt would be to construct weight functions for which their sum (A + B) is always equal to 1 for each $\alpha \in [0, \pi/2]$. Fig. 16 represents two possible solutions of weight functions, one linear and one non-linear, that respect the aforementioned constraints; however, multiple (theoretically infinite) alternatives exist.

The minimum load factor λ_α capable of activating the failure mechanism is computed through an optimisation routine that can explore the

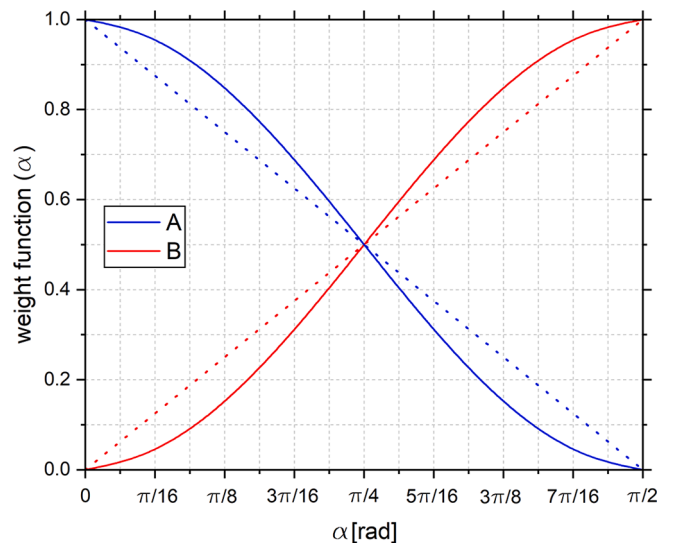


Fig. 16. Possible alternative of weight functions.

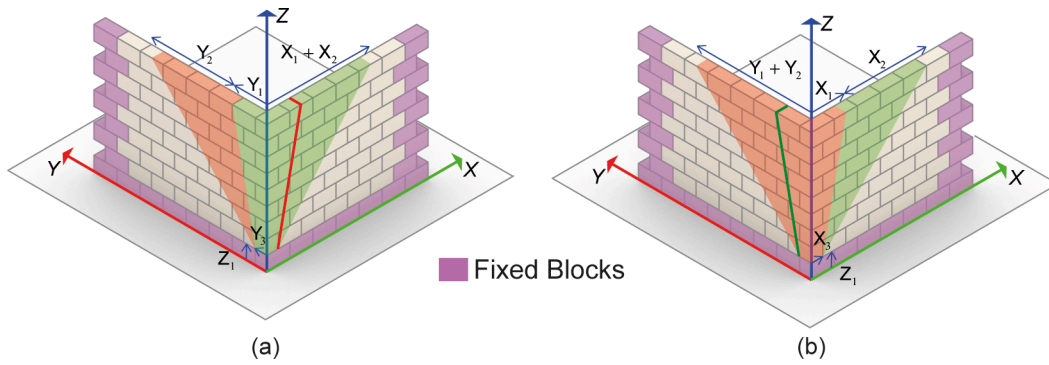


Fig. 17. Definition of the failure mechanism: (a) macroblock parametrisation related to the computation of λ_X and (b) macroblock parametrisation related to the computation of λ_Y .

whole possible range of solutions by modifying the geometry of the failure mechanism, always respecting the kinematic mechanism reported in Fig. 15. Fig. 17 represents the parametrisation of the mechanism geometry as a function of the optimisation variables.

It is worth noting that the optimisation variable has to respect conditions of geometric compatibility depending on the overall dimension of the corner prototype as well as the dimensions of the blocks. Finally, the optimisation of the failure mechanism geometry is achieved by solving the following constrained minimisation problem:

minimise : $\lambda_\alpha(\lambda_X, \lambda_Y)$
 subject to: $h \leq Z_1 \leq H$
 $Y_3 \geq t_Y$
 $Y_3 \leq Y_2$
 $Y_1 + Y_2 \leq L_{WY}$
 $\frac{Y_1 + Y_2 - Y_3}{H - Z_1} \leq \tan \alpha_b$ (13)
 $X_3 \geq t_X$
 $X_3 \leq X_1$
 $X_1 + X_2 \leq L_{WX}$
 $\frac{X_1 + X_2 - X_3}{H - Z_1} \leq \tan \alpha_b$

where, $X_1, X_2, X_3, Y_1, Y_2, Y_3$ and Z_1 are the dimensions that define the size of the macroblocks (Fig. 17), H is the height of the corner prototype, while L_W and t are the length and the thickness of the wall along the X and Y axes (defined by the subscript X or Y), respectively. This constrained optimisation problem has been mathematically implemented in a GHPython script [59,60]. The solution is achieved using a heuristic solver based on the Nelder-Mead method [61] that is able to refine the geometry of the macroblocks and search for the minimum value of the load multiplier λ_α within a few seconds.

4.2. Experimental and numerical validation

The analytical model has been validated against the obtained experimental and numerical results reported in Sections 2.3 and 3.2. According to the experimental tests and the numerical model, the dimensions of the blocks are consistent with those reported in Section 2.1, whereas the friction coefficient has been set to the value of $\mu = 0.66$ ($\varphi = 34^\circ$). In this case, the weight functions are assumed as equal to $A = \cos^2(\alpha)$ and $B = \sin^2(\alpha)$. Concerning the horizontal flexural mechanism, the k parameter (reducing the frictional forces due to uplift of blocks) has been set to vary from 0.3 to 0.6, which corresponds to a reasonable range of values according to [15].

The analytical model results, which are reported for both horizontal flexural and pure rocking-sliding mechanisms, have been evaluated in

Table 5 Comparison of the experimental and numerical load multipliers λ_α , with Difference (%) = $(\lambda_\alpha^{LA} - \lambda_\alpha^{EXP})/\lambda_\alpha^{EXP} \times 100$.

Load orientation α	Load Multiplier λ_α		Difference (%)
	Experimental	LA $k = 0.3$	
$\pi/4$	0.287	0.290	1.0
$5\pi/16$	0.270	0.284	5.2
$3\pi/8$	0.248	0.263	6.0
$7\pi/16$	0.239	0.238	-0.4
$\pi/2$	0.236	0.229	-3.0

terms of the load multipliers λ_α and associated collapse mechanisms obtained for each load orientation angle α . As Table 5 and Fig. 18 indicate, the horizontal flexural results better fit the experimental data, with overestimations only for $\alpha = 5\pi/16$ and $\alpha = 3\pi/8$. This effect might be easily corrected by assuming other weight functions that better approximate the experimental results, though such optimisation is out of the scope of the present paper.

Regarding the collapse mechanisms, Fig. 19 shows the geometry of the macroblock involved for the range of experimentally investigated angles. It is worth highlighting the good agreement between the macroblock geometries reported in Fig. 19 and the blocks involved in the collapse mechanisms in the experimental tests and numerical simulations, as illustrated in Fig. 6 and Fig. 12. One can note how the analytical model predicts a symmetric macroblock geometry when $\alpha = \pi/4$,

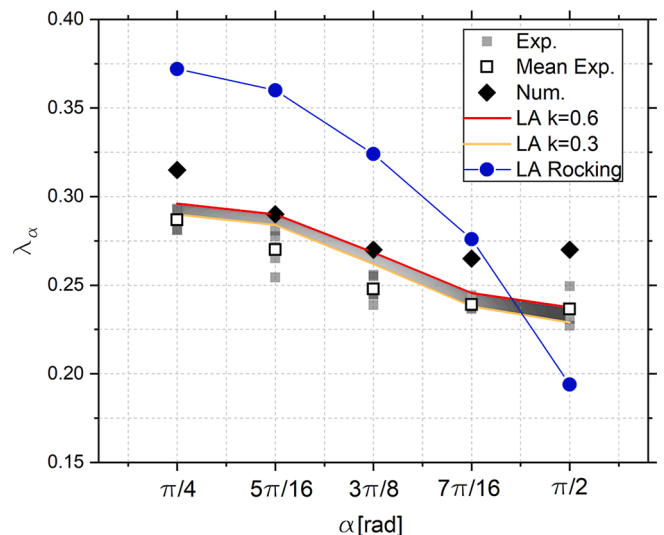


Fig. 18. Variation of collapse load multiplier with load orientation for the experimental tests, numerical and analytical models.

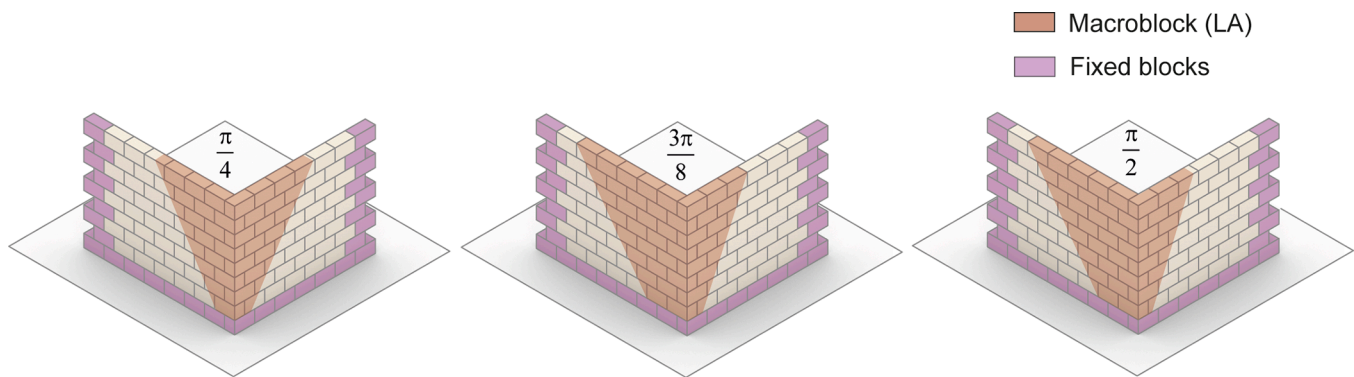


Fig. 19. Macroblock mechanisms obtained by LA, for the different load orientations.

whereas, as in the case of the experimental results, by increasing α until $\pi/2$ the walls influenced by predominant out-of-plane and in-plane effects tend to increase and decrease their dimensions, respectively.

The obtained results in terms of the horizontal load multiplier and collapse mechanism of the macroblock demonstrate the adequacy of the proposed analytical model.

5. Final remarks

This paper presented the results of experimental, numerical, and analytical investigations into the failure of masonry corners subjected to lateral loading due to seismic action. An experimental tilting table campaign was conducted on dry-joint masonry corners in order to gain a more comprehensive understanding of this less understood failure mechanism that commonly occurs during earthquakes. In particular, the effect of the seismic load orientation has been investigated here for the first time. The experimental data, including the material characterisation, served to validate numerical DEM and analytical LA approaches. Both methods can be readily used to carry out parametric analyses on similar configurations (to investigate, for example, the effect of masonry arrangement, axial overload and the presence of openings) and/or to assess the seismic stability of larger-scale masonry buildings. While these additional analyses are beyond the scope of the current paper, they should be addressed in future works.

The following points summarise the main findings and contributions of the paper:

- The experimental characterisation of the dry-joint masonry included less commonly investigated parameters, namely the dry-joint stiffnesses. The results have shown that the commonly used linearly proportional normal stiffness with normal stress approximates the dry-joint behaviour well. However, the numerical simulations evidenced that the actual joint stiffness in a full wall might be smaller (by a factor of 2 to 3) than the one obtained from a joint closure tests using only two blocks. These outcomes can be used for other experimental studies of dry-joint properties and can also serve as a reference for numerical simulations that do not have access to the actual joint stiffness.
- The paper highlighted the effect of the seismic orientation on the collapse load multiplier and the collapse mechanism. It has been observed that the loading case $\pi/4$ (when the pseudo-static action symmetrically loads the corner) has the highest resistance to collapse, while the loading case $\pi/2$ is the most critical one. Furthermore, the collapse mechanism of the $\pi/2$ loading case clearly showed that the rocking-sliding and flexural mechanisms occur simultaneously, with the out-of-plane loaded wall experiencing a pure flexural mechanism and the in-plane loaded wall experiencing pure rocking-sliding motion. When the orientation rotates from $\pi/2$ to $\pi/4$, the flexural mechanism appears progressively in the mostly

in-plane loaded wall, while rocking-sliding is noticeable in the mostly out-of-plane loaded wall. Both collapse mechanisms and collapse load multipliers have been found to be repeatable, highlighting the quality of the experimental data that can be readily used for other studies.

- The paper re-iterated the ability of Discrete Element simulations to reproduce the results of experimental tests on dry-joint masonry structures both in terms of collapse mechanisms and their associated collapse load multipliers. In the original case, no numerical calibration of parameters was carried out, and only the experimental data was used, resulting in an average overestimation of the ultimate load of 10%. However, further investigations into the wall slenderness and joint stiffness highlighted the sensitivity of the results – particularly the collapse load multiplier – to these parameters. Specifically, a reduction of the joint stiffness by 50% was found to better capture the experimental results (average error of 4%), thereby stressing the importance of identifying this parameter on masonry walls as a whole and not only with joint closure tests.
- The work introduced a new LA model that accounts for rocking-sliding and flexural mechanisms. Results demonstrated that the analytical model describes the experimental results well, both in terms of load multiplier and macroblocks involved in the mechanism. Only slight overestimations (Difference (%) \simeq 5%) for $\alpha = 5\pi/16$ and $\alpha = 3\pi/8$ were predicted.

CRediT authorship contribution statement

Carla Colombo: Methodology, Writing – original draft, Visualization. **Nathanaël Savalle:** Methodology, Conceptualization, Supervision, Writing – original draft. **Anjali Mehrotra:** Methodology, Conceptualization, Writing – original draft. **Marco Francesco Funari:** Methodology, Conceptualization, Writing – original draft, Supervision, Visualization. **Paulo B. Lourenço:** Writing – review & editing, Supervision.

Declaration of Competing Interest

The authors declare the following financial interests/personal relationships which may be considered as potential competing interests: Paulo B. Lourenço reports financial support was provided by European Research Council (ERC). Paulo B. Lourenço belongs to the Editorial Advisory Board of Construction and Building Materials Journal.

Acknowledgements

The authors want to greatly acknowledge the technical support of UMinho laboratory staff. Similarly, the authors also want to thank all STAND4HERITAGE team for the valuable scientific discussions on the

subject. Finally, the authors are grateful to the Xella company who provided the masonry units.

Funding

This work was partly financed by FCT/MCTES through national funds (PIDDAC) under the R&D Unit Institute for Sustainability and Innovation in Structural Engineering (ISISE), under reference UIDB/04029/2020. This study has been partly funded by the STAND4-HERITAGE project (New Standards for Seismic Assessment of Built Cultural Heritage) that has received funding from the European Research Council (ERC) under the European Union's Horizon 2020 research and innovation programme (Grant agreement No. 833123), as an Advanced Grant.

References

- [1] L. Lulić, K. Ožić, T. Kišiček, I. Hafner, and M. Stepinac. "Post-Earthquake Damage Assessment—Case Study of the Educational Building after the Zagreb Earthquake," *Sustain.* 2021. Vol. 13. Page 6353. vol. 13. no. 11. p. 6353. Jun. 2021. doi: 10.3390/SU13116353.
- [2] G. Vlachakis, E. Vlachaki, P.B. Lourenço, Learning from failure: Damage and failure of masonry structures, after the 2017 Lesvos earthquake (Greece), *Eng. Fail. Anal.* 117 (July) (2020), 104803, <https://doi.org/10.1016/j.engfailanal.2020.104803>.
- [3] A. Giuffrè, "A Mechanical Model for Statics and Dynamics of Historical Masonry Buildings", in: *Protection of the Architectural Heritage Against Earthquakes*, Springer, Vienna, 1996, pp. 71–152.
- [4] J. Heyman, The stone skeleton, *Int. J. Solids Struct.* 2 (2) (1966) 249–279, [https://doi.org/10.1016/0020-7683\(66\)90018-7](https://doi.org/10.1016/0020-7683(66)90018-7).
- [5] D. D'Ayala, E. Speranza, Definition of Collapse Mechanisms and Seismic Vulnerability of Historic Masonry Buildings, *Earthq. Spectra* 19 (3) (2003) 479–509, <https://doi.org/10.1193/1.1599896>.
- [6] P. Block, T. Ciblac, J. Ochsendorf, Real-time limit analysis of vaulted masonry buildings, *Comput. Struct.* 84 (29–30) (2006) 1841–1852, <https://doi.org/10.1016/J.COMPSTRUC.2006.08.002>.
- [7] M. F. Funari, L. C. Silva, E. Mousavian, and P. B. Lourenço, "Real-time Structural Stability of Domes through Limit Analysis: Application to St. Peter's Dome." <https://doi.org/10.1080/15583058.2021.1992539>. pp. 1–23. Oct. 2021. doi: 10.1080/15583058.2021.1992539.
- [8] F. Portioli, C. Casapulla, M. Gilbert, L. Cascini, Limit Analysis Of 3D Masonry Block Structures With Non-Associative Frictional Joints Using Cone Programming, *Comput. Struct.* 84 (13–14) (2006) 873–887.
- [9] N. Isand, N. Khattak, Observed failure modes of unreinforced masonry buildings during the 2015 Hindu Kush earthquake, *Earthq. Eng. Eng. Vib.* 18 (2) (2019) 301–314, <https://doi.org/10.1007/s11803-019-0505-x>.
- [10] M. Stepinac, P.B. Lourenço, J. Atalić, T. Kišiček, M. Uroš, M. Baniček, M. Šavor Novak, Damage classification of residential buildings in historical downtown after the ML5.5 earthquake in Zagreb, Croatia in 2020, *International Journal of Disaster Risk Reduction* 56 (2021) 102140.
- [11] C. Casapulla, A. Maione, L.U. Argiento, E. Speranza, Corner failure in masonry buildings: An updated macro-modeling approach with frictional resistances, *Eur. J. Mech. A/Solids* 70 (March) (2018) 213–225, <https://doi.org/10.1016/j.euromechsol.2018.03.003>.
- [12] C. Casapulla, L. U. Argiento, A. Maione, and E. Speranza, "Upgraded formulations for the onset of local mechanisms in multi-storey masonry buildings using limit analysis," *Structures*, vol. 31, no. November 2020, pp. 380–394, 2021, doi: 10.1016/j.istruc.2020.11.083.
- [13] C. Casapulla, L. Giresini, L.U. Argiento, A. Maione, Nonlinear Static and Dynamic Analysis of Rocking Masonry Corners Using Rigid Macro-Block Modeling, *Int. J. Str. Stab. Dyn.* 19 (11) (2019) 1950137.
- [14] M.F. Funari, A. Mehrotra, P.B. Lourenço, A Tool for the Rapid Seismic Assessment of Historic Masonry Structures Based on Limit Analysis Optimisation and Rocking Dynamics, *Appl. Sci.* 11 (3) (2021) 942, <https://doi.org/10.3390/app11030942>.
- [15] C. Casapulla, A. Maione, Experimental and Analytical Investigation on the Corner Failure in Masonry Buildings: Interaction between Rocking-Sliding and Horizontal Flexure, *Int. J. Archit. Herit.* 14 (2) (2018) 208–220, <https://doi.org/10.1080/15583058.2018.1529206>.
- [16] A. Aşıkoglu, Ö. Avşar, P.B. Lourenço, L.C. Silva, Effectiveness of seismic retrofitting of a historical masonry structure: Kütahya Kurşunlu Mosque, Turkey, *Bull. Earthq. Eng.* 17 (6) (2019) 3365–3395, <https://doi.org/10.1007/s10518-019-00603-6>.
- [17] G. Fortunato, M.F. Funari, P. Lonetti, Survey and seismic vulnerability assessment of the Baptistery of San Giovanni in Tumba (Italy), *J. Cult. Herit.* 26 (2017) 64–78.
- [18] M. Betti, L. Galano, Seismic analysis of historic masonry buildings: The Vicarious Palace in Pescia (Italy), *Buildings* 2 (2) (2012) 63–82, <https://doi.org/10.3390/buildings20020063>.
- [19] H. Smoljanović, N. Živaljić, Ž. Nikolić, A. Munjiza, Numerical analysis of 3D dry-stone masonry structures by combined finite-discrete element method, *Int. J. Solids Struct.* 136–137 (2018) 150–167, <https://doi.org/10.1016/j.ijsolstr.2017.12.012>.
- [20] J.V. Lemos, Discrete element modeling of masonry structures, *Int. J. Archit. Herit.* 1 (2) (2007) 190–213, <https://doi.org/10.1080/15583050601176868>.
- [21] J. V. Lemos. "Discrete element modeling of the seismic behavior of masonry construction." *Buildings*. vol. 9. no. 2. 2019. doi: 10.3390/buildings9020043.
- [22] T.T. Bui, A. Limam, V. Sarhosis, M. Hjiatj, Discrete element modelling of the in-plane and out-of-plane behaviour of dry-joint masonry wall constructions, *Eng. Struct.* 136 (2017) 277–294, <https://doi.org/10.1016/j.engstruct.2017.01.020>.
- [23] S. Gonen, B. Pulatsu, E. Erdogmus, E. Karaesmen, E. Karaesmen, Quasi-static nonlinear seismic assessment of a fourth century A.D. Roman Aqueduct in Istanbul, Turkey, *Heritage* 4 (1) (2021) 401–421, <https://doi.org/10.3390/heritage4010025>.
- [24] N. Savalle, É. Vincens, S. Hans, Experimental and numerical studies on scaled-down dry-joint retaining walls: Pseudo-static approach to quantify the resistance of a dry-joint brick retaining wall, *Bull. Earthq. Eng.* 18 (2) (2020) 581–606, <https://doi.org/10.1007/s10518-019-00670-9>.
- [25] P.B. Lourenço, Computations on historic masonry structures, *Prog. Struct. Eng. Mater.* 4 (3) (2002) 301–319, <https://doi.org/10.1002/pse.120>.
- [26] A.P. Alexandris, E. Protopapa, I. Psycharis, Collapse mechanisms of masonry buildings driven by the distinct element method, 3th World Conf. Earthq. Eng. 548 (2004) p. No.548.
- [27] T. T. Bui and A. Limam. "Masonry Walls under Membrane or Bending Loading Cases : Experiments and Discrete Element Analysis." In *Proceedings of the Eleventh International Conference on Computational Structures Technology*. 2012. p. Paper 119.
- [28] G. De Felice, R. Giannini, Out-of-plane seismic resistance of masonry walls, *J. Earthq. Eng.* 5 (2) (2001) 253–271, <https://doi.org/10.1080/13632460109350394>.
- [29] J.V. Lemos, A. Campos Costa, Simulation of Shake Table Tests on Out-of-Plane Masonry Buildings. Part (V): Discrete Element Approach, *Int. J. Archit. Herit.* 11 (1) (2017) 117–124, <https://doi.org/10.1080/15583058.2016.1237587>.
- [30] O. Al Shawa, G. de Felice, A. Mauro, L. Sorrentino, Out-of-plane seismic behaviour of rocking masonry walls, *Earthq. Eng. Struct. Dyn.* 41 (2012) 949–968, <https://doi.org/10.1002/eqe>.
- [31] Y. Zhuge, Distinct element modelling of unreinforced masonry wall under seismic loads with and without cable retrofitting, *Trans. Tianjin Univ.* 14 (S1) (2008) 471–475, <https://doi.org/10.1007/s12209-008-0080-0>.
- [32] T. Forgács, V. Sarhosis, K. Bagi, Influence of construction method on the load bearing capacity of skew masonry arches, *Eng. Struct.* 168 (2018) 612–627, <https://doi.org/10.1016/j.engstruct.2018.05.005>.
- [33] B. Pulatsu, E. Erdogmus, J. V Lemos, and K. Tuncay. "Simulation of the In-Plane Structural Behavior of Unreinforced Masonry Walls and Buildings using DEM." vol. 27. pp. 2274–2287. 2020. doi: 10.1016/j.istruc.2020.08.026.1.
- [34] P.B. Lourenço, L.C. Silva, Computational applications in masonry structures: From the meso-scale to the super-large/super-complex, *Int. J. Multiscale Comput. Eng.* 18 (1) (2020) 1–30, <https://doi.org/10.1615/IntJMultCompEng.2020030889>.
- [35] M.F. Funari, S. Spadea, P. Lonetti, F. Fabbrocino, R. Luciano, Visual programming for structural assessment of out-of-plane mechanisms in historic masonry structures, *J. Build. Eng.* vol. 31, no. April (2020), 101425, <https://doi.org/10.1016/j.jobe.2020.101425>.
- [36] G. Castellazzi, A.M. D'Altri, G. Bitelli, I. Selvaggi, A. Lambertini, From laser scanning to finite element analysis of complex buildings by using a semi-automatic procedure, *Sensors (Switzerland)* 15 (8) (2015) 18360–18380, <https://doi.org/10.3390/s150818360>.
- [37] M. F. Funari, L. C. Silva, N. Savalle, and P. B. Lourenço, "A concurrent micro/macro FE-model optimized with a limit analysis tool for the assessment of dry-joint masonry structures," *Int. J. Multiscale Comput. Eng.*, vol. In Press, 2022, doi: 10.1615/IntJMultCompEng.2021040212.
- [38] F. Vadalà, V. Cusmano, M.F. Funari, I. Calìo, P.B. Lourenço, On the use of a mesoscale masonry pattern representation in discrete macro-element approach, *J. Build. Eng.* 50 (2022), 104182, <https://doi.org/10.1016/j.jobe.2022.104182>.
- [39] "XELLA Company, Silka blocks." <https://www.xella.com/en/US/>.
- [40] ASTM D 2938-02. "Standard test method for Unconfined Compressive Strength of Intact Rock Core Specimens." *Am. Soc. Test. Mater.* no. D2938-95. 1–3. 1995.
- [41] ASTM D 3148-02. "Standard test method for elastic moduli of rock core specimens in uniaxial compression," *Am. Soc. Test. Mater.*, no. D 3148-02, pp. 138–140, 2002.
- [42] P.H.S.W. Kulatilake, S. Shreedharan, T. Sherizadeh, B. Shu, Y. Xing, P. He, Laboratory Estimation of Rock Joint Stiffness and Frictional Parameters, *Geotech. Geol. Eng.* 34 (6) (2016) 1723–1735, <https://doi.org/10.1007/s10706-016-9984-y>.
- [43] W.A.M. Thanoon, A.H. Alwathaf, J. Noorzai, M.S. Jaafar, M.R. Abdulkadir, Finite element analysis of interlocking mortarless hollow block masonry prism, *Comput. Struct.* 86 (6) (2008) 520–528, <https://doi.org/10.1016/j.compstruc.2007.05.022>.
- [44] R.L.G. Oliveira, J.P.C. Rodrigues, J.M. Pereira, P.B. Lourenço, H. Ulrich Marschall, Normal and tangential behaviour of dry joints in refractory masonry, *Engineering Structures* 243 (2021) 112600.
- [45] P.M. Naik, T. Bhowmik, A. Menon, Estimating joint stiffness and friction parameters for dry stone masonry constructions, *Int. J. Mason. Res. Innov.* 1 (1) (2020) 1, <https://doi.org/10.1504/ijmri.2020.10033088>.
- [46] K. Andreev, S. Sinnema, A. Reik, S. Allaoui, E. Blond, A. Gasser, Compressive behaviour of dry joints in refractory ceramic masonry, *Constr. Build. Mater.* 34 (2012) 402–408, <https://doi.org/10.1016/j.conbuildmat.2012.02.024>.
- [47] M.E. Kartal, D.M. Mulvihill, D. Nowell, D.A. Hills, Determination of the Frictional Properties of Titanium and Nickel Alloys Using the Digital Image Correlation Method, *Exp. Mech.* 51 (3) (2011) 359–371, <https://doi.org/10.1007/s11340-010-9366-y>.
- [48] A. Fantetti, L.R. Tamatam, M. Volvert, I. Lawal, L. Liu, L. Salles, M.R.W. Brake, C. W. Schwingshackl, D. Nowell, The impact of fretting wear on structural dynamics: Experiment and Simulation, *Tribol. Int.* 138 (2019) 111–124.

- [49] P. Lourenço, L. Ramos, Characterization of cyclic behavior of dry masonry joints, *J. Struct. Eng.* 5 (130) (2004) 779–786.
- [50] S. Biwa, S. Hiraiwa, E. Matsumoto, Stiffness evaluation of contacting surfaces by bulk and interface waves, *Ultrasonics* 47 (1–4) (2007) 123–129, <https://doi.org/10.1016/j.ultras.2007.08.005>.
- [51] C. Campañá, B.N.J. Persson, M.H. Müser, Transverse and normal interfacial stiffness of solids with randomly rough surfaces, *J. Phys.: Condens. Matter* 23 (8) (2011) 085001.
- [52] BS EN 1052-3. “Methods of test for masonry – Part 3: Determination of initial shear strength,” *BSi – British Stand.*, p. 18. 2002.
- [53] Y. Shi, D. D’Ayala, and J. Prateek. “Analysis of out-of-plane damage behaviour of unreinforced masonry walls.” In *14th international brick and block masonry conference*. 2008. pp. 02–17.
- [54] L.F. Restrepo Vélez, G. Magenes, M.C. Griffith, Dry stone masonry walls in bending-Part I: Static tests, *Int. J. Archit. Herit.* 8 (1) (2014) 1–28, <https://doi.org/10.1080/15583058.2012.663059>.
- [55] “Colombo, Carla, Funari, Marco Francesco, Savalle, Nathanaël, & Lourenço, Paulo B. (2021). Tilting test campaign on masonry corners (2021-06-03, UMinho) <https://doi.org/10.5281/zenodo.5572624>”.
- [56] C. Colombo, L. Fernandes, N. Savalle, and P. B. Lourenço. “Tilting tests for masonry structures: design and preliminary numerical modelling.” In *14th Canadian Masonry Symposium*. 2021. pp. 1–11.
- [57] Itasca Consulting Group Inc., *3DEC – Three-Dimensional Distinct Element Code, Ver. 7.0: Theory and Background*. 2019.
- [58] C. Casapulla, L.U. Argiento, In-plane frictional resistances in dry block masonry walls and rocking-sliding failure modes revisited and experimentally validated, *Compos. Part B Eng.* 132 (2018) 197–213, <https://doi.org/10.1016/J.COMPOSITESB.2017.09.013>.
- [59] “Grasshopper – Algorithmic modeling for Rhino.” 2020.
- [60] “The Python Language Reference — Python 3.9.5 documentation”.
- [61] J.C. Lagarias, J.A. Reeds, M.H. Wright, P.E. Wright, Convergence properties of the Nelder-Mead simplex method in low dimensions, *SIAM J. Optim.* 9 (1) (1998) 112–147.